Enhanced Charge Carrier Mobility in Two-Dimensional High Dielectric Molybdenum Oxide

Sivacarendran Balendhran, Junkai Deng, Jian Zhen Ou, Sumeet Walia, James Scott, Jianshi Tang, Kang L. Wang, Matthew R. Field, Salvy Russo, Serge Zhuiykov, Michael S. Strano, Nikhil Medhekar,* Sharath Sriram, Madhu Bhaskaran,* and Kourosh Kalantar-zadeh**

In atomically thin two-dimensional (2D) materials, free charges have quantized energy levels in one spatial dimension, while they are mobile in the other two.[1] The interest in such 2D materials increased in the late 1970s and early 1980s driven by a large amount of experimental outcomes from the development of molecular beam epitaxy (MBE) equipment for the deposition of high quality thin films of III-V semiconductors.[2] This resulted in the realization of high electron mobility transistors, with thin films of different bandgaps that can operate at very high frequencies. In such devices, the conduction band energy of at least one of the films is forced under the Fermi level at the junction, creating a narrow quantum well, and the quantization of free charges.[3] Such structures can offer electron mobilities larger than 10^6 cm^2 V^{-1} s^{-1} (at near zero Kelvin temperatures), which is significantly larger than that of silicon.[4] However, the high cost of the rare-earth materials, lack of compatibility, and technological difficulties for creating III-V structures hinders their widespread adaptation.

The emergence of graphene has revived the interest in 2D materials, due to its many favorable properties including enhanced electron mobilities that exceed 10^5 cm^2 V^{-1} s^{-1}.[5] However, graphene lacks the semiconducting characteristics of prevalent materials, such as silicon with their natural energy bandgap.[5,6] Even though there have been advancements in introducing a bandgap to graphene,[7] the required complex synthesis processes always resulted in significant loss in the much desired carrier mobilities.[8] It is suggested that alternative layered materials such as semiconducting transition metal dichalcogenides (e.g., molybdenum disulfide–MoS_2 – one of the most researched in this group) would solve the issue of introducing a bandgap, but still results in relatively low carrier mobilities.[9,10] Recent reports on atomically thin MoS_2 indicate possible approaches to increase its mobility by introducing a high dielectric top-gate material (HfO_2) that reduces Coulomb scattering to attain values smaller than 220 cm^2 V^{-1} s^{-1}, which is still less than values sought after.[10]

In this work, we propose that 2D semiconducting metal oxides with high dielectric constant (high-κ) offer a solution for obtaining high electron mobility.[11–13] Advantageously, the electronic properties, in particular the bandgap, of such 2D metal oxides can be largely manipulated using well-known chemical and physical approaches.[13] Such manipulations, which impose their effects on the 2D environment, categorize these materials as excellent templates for achieving the optimum quantum parameters required for target applications. The charge mobility in a thin layer is calculated using $\mu = \frac{e}{m^*}\langle\tau\rangle$, in which e is the point charge, τ is the transport relaxation rate of momentum in the plane, and m^* is the electron effective mass. Considering Born approximation, the transport relaxation time is calculated using:[2]

$$\frac{1}{\tau(E_k)} = \frac{2\pi}{\hbar}\sum_{k_z}\sum_{\mu}\int_{-\infty}^{+\infty} N_i^{(\mu)}(z)\left|V_{k-k_z}^{(\mu)}(z)\right|^2 \times\left(1-\cos\theta_{kk_z}\right)\times\delta\left(E(k)-E(k_z)\right) \quad (1)$$

S. Balendhran, J. Z. Ou, S. Walia, Prof. J. Scott,
Dr. S. Sriram, Dr. M. Bhaskaran, Prof. K. Kalantar-zadeh
MicroNanoElectronics and Sensor Technology
Research Group and Functional Materials and
Microsystems Research Group
School of Electrical and Computer Engineering
RMIT University
Melbourne, Victoria, Australia
E-mail: shiva.balendhran@rmit.edu.au;
madhu.bhaskaran@rmit.edu.au; kourosh.kalantar@rmit.edu.au

Dr. J. Deng, Dr. N. Medhekar
Department of Materials Engineering
Monash University
Clayton, Victoria, Australia
E-mail: nikhil.medhekar@monash.edu

J. Tang, Prof. K. L. Wang
Device Research Laboratory
Department of Electrical Engineering
University of California, Los Angeles, California, USA

Dr. M. R. Field, Prof. S. Russo
School of Applied Sciences
RMIT University, Melbourne
Victoria, Australia

Dr. S. Zhuiykov
Materials Science and Engineering Division
CSIRO, Highett, Victoria, Australia

Prof. M. S. Strano
Department of Chemical Engineering
Massachusetts Institute of Technology
Cambridge, Massachusetts, USA

DOI: 10.1002/adma.201203346

in which $N^{(\mu)}{}_i(z)$ is the concentration of the μ^{th} kind of Coulomb charge center and θ_{kk_z} is the angle between k and k_z vectors. $V^{(\mu)}_{k-k_z}(z)$ is a potential function showing the intensity of the scattering effects on free mobile charges, and the reduction of $V^{(\mu)}_{k-k_z}(z)$ is important in obtaining large carrier mobilities. The term $V^{(\mu)}_{k-k_z}(z)$ is a function of many parameters of the material and its surrounding environment such as permittivity, temperature, 2D material thickness, embedded charges, and electronic structure of the material. Its presence provides many degrees of freedom for manipulating the properties of the 2D material. In metal oxides of high relative dielectric constants, such as α-MoO_3, the overall effect of Coulomb charges on $V^{(\mu)}_{k-k_z}(z)$ is reduced and according to Equation 1 the scattering effect will be dominated by the optical and acoustic phonons. This is due to the fact that in a 2D semiconductor the permittivity appears in the denominator of the potential function.[2] For instance at room temperature, for a 2D material with a κ of 5 and a thickness of 11 nm the mobility is approximately ~170 $cm^2\ V^{-1}\ s^{-1}$, while for a material of the same thickness and a high-κ of 500, this number advantageously increases to ~3200 $cm^2\ V^{-1}\ s^{-1}$ which is limited by acoustic scattering rather than Coulomb scattering (see supporting information). Many transition metal dichalcogenides have small relative dielectric constants (e.g. ~5 for MoS_2).[14] In contrast, many semiconducting metal oxides, such as α-MoO_3, possess much larger relative dielectric constants (>500 for α-MoO_3).[15] Also favorably, α-MoO_3's structure is made of perfect planar crystals, held together by van der Waals forces (**Figure 1**a), which also offers the possibility of obtaining 2D structures using various exfoliation methods.[11] At a level of few layers, the dielectric value can be reduced in comparison to its bulk counterpart (see supporting information).[16] However, this reduced value had a negligible effect on the overall charge mobility of our device, as the acoustic scattering still remains the main limiting factor at and above room temperature.

MoO_3, in its intrinsic form, has a wide bandgap (>2.7 eV) resulting in a low carrier concentration, which is not suitable for electronic devices.[17] It is well known that α-MoO_3 can be reduced to form $MoO_{(3-x)}$ and increasing x can lower the bandgap.[18,19] We have previously demonstrated that intercalating ions such as H^+ can interact with oxygen atoms of α-MoO_3, gradually leaving the material as H_2O vapor, and result in oxygen deficiencies.[20] In low-κ materials, this process increases the number of embedded Coulomb charges and has a possible detrimental effect on electron scattering. On the contrary, according to Equation 1, as α-MoO_3 is a layered high-κ material, the Coulomb scattering effect is minimal and acoustic phonon scattering has the most impact at room temperature.[2]

We extensively investigated the reduction process of α-MoO_3 flakes to gain perfect control of the Coulomb charge

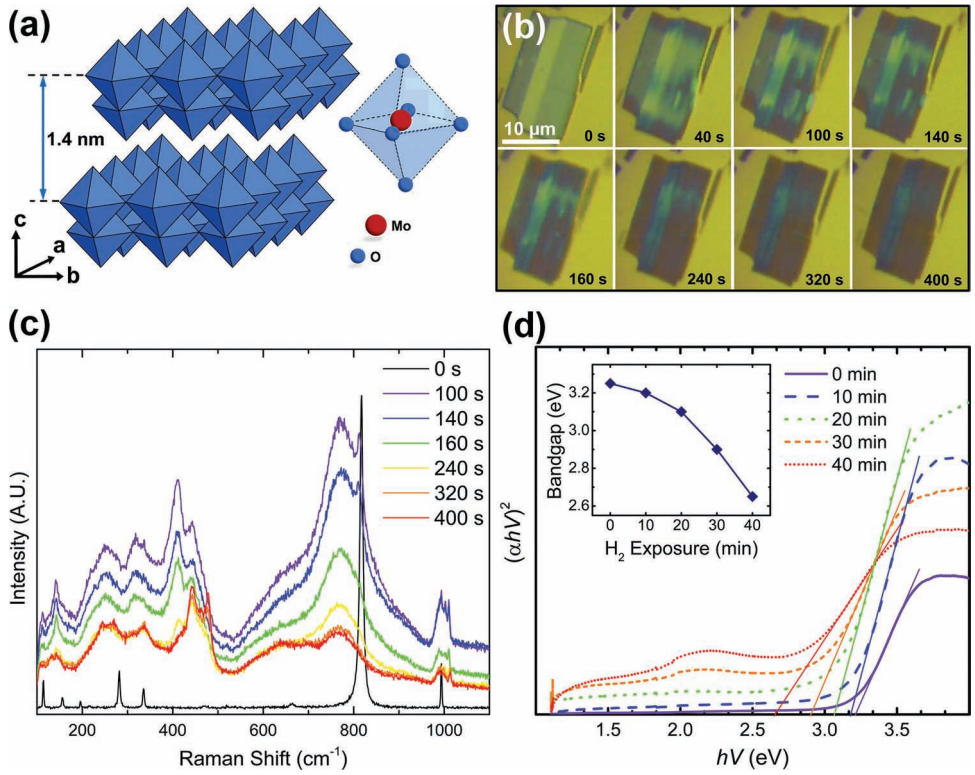

Figure 1. MoO_3 crystal structure and intercalation for sub-stoichiometry. (a) 1.4 nm octahedral structures held together by van der Waals forces. (b) Optical microscopy images showing evolution of a thin MoO_3 flake with duration of H^+ intercalation. (c) Micro-Raman spectra corresponding to optical images in (b). (d) Photon energy vs. $(\alpha h\nu)^2$ curves derived from the absorbance spectrum of a MoO_3 flake with progression of catalyzed H^+ intercalation. Intersection of the linear fit with the x–axis indicates the bandgap energy, used to depict the change in estimated optical bandgap with progression of the intercalation process (inset). The measurement for (d) was performed by intercalating thicker flakes in order to observe changes in the absorbance spectra.

incorporation process. Flakes of stratified α-MoO_3 was synthesized through thermal evaporation of MoO_3 powder, followed by mechanical exfoliation to realize perfect α-MoO_3 planar crystals (Figures S2–S4).[11] We studied the intercalation in these layers *via* their exposure to H^+ ions.[20] Similar intercalation behavior was also observed upon exposure to H_2 gas, as H_2 readily breaks onto the MoO_3 surface to form H^+ ions (Figures S5 and S6). However, the H_2 gas exposure procedure has an advantage as H_yMoO_3 readily loses H_2O to ambient, producing the desired sub-stoichiometry $MoO_{(3-x)}$.[20] The electronic behavior of H_yMoO_3 and $MoO_{(3-x)}$ are similar as they both have the same number of Coulomb charges. Similarly, highly energetic beams and annealing in a high vacuum environment can also reduce the material.[21] So any of the aforementioned methods can be equally used for obtaining $MoO_{(3-x)}$. In brief, by introducing the oxygen vacancies, Mo^{6+} neighboring the oxygen vacancies in the MoO_3 lattice would be reduced to Mo^{5+}, injecting an electron to the conduction band.[18,21] The additional electron from such Mo^{5+} is delocalized within the layers, since it is not tightly bound to any Mo^{6+} core cation. This will give rise to a gap state in between the valence and conduction bands of MoO_3 hence narrowing its band gap.

Optical images of an α-MoO_3 flake (Figure 1b) show the progress of the liquid phase intercalation with time, generating a change of appearance from transparent to Prussian blue. Raman spectra of the same flake reveal the evolution of the $MoO_{(3-x)}$ from the α-MoO_3 (Figure 1c), based on the fact that the sharp peak of MoO_3 at 820 cm^{-1} gradually disappeared, and a broad peak at ~780 cm^{-1} emerged instead. The Raman peak shift at 780 cm^{-1} is a strong indication for the presence and strength of sub-stoichiometric crystal formation.[20] The bandgap reduced from 3.25 to 2.65eV after exposure to H_2 gas (Figure 1d) and to smaller values less than 2 eV afterwards (which can be extrapolated). Collectively, these results confirm the presence of sub-stoichiometric $MoO_{(3-x)}$, and the ability to reduce bandgap as a function of x. In this work, the aforementioned process is adopted to reduce stoichiometry in thin layers of molybdenum oxide, in order to produce a 2D layer with reduced bandgap and large electron concentration, hence making it suitable for FET applications.

The flakes were mechanically exfoliated onto 300 nm SiO_2 on highly p-doped Si substrates as well as on Si substrates with an optically smooth gold layer. Transmission electron microscopy (TEM) image of a flake before exfoliation (**Figure 2**a) and scanning tunneling microscopy (STM) image after the exfoliation (Figure 2b) show parallel lattice fringes with spacing of 0.39 nm, which is also in agreement with the STMs for both before and after losing H_2O.(see supporting information) These indicate perfect crystallinity of the layers and also perfectly matched crystal lattices of MoO_3 and $MoO_{(3-x)}$.

In order to fabricate field effect transistors (FETs) with thin layered oxide and assess the charge carrier mobility, the thickness of the exfoliated layers were identified using scanning electron microscopy (SEM) and atomic force microscopy (AFM). Platinum/gold electrodes were formed using a combination of electron beam lithography and photolithography. See Materials

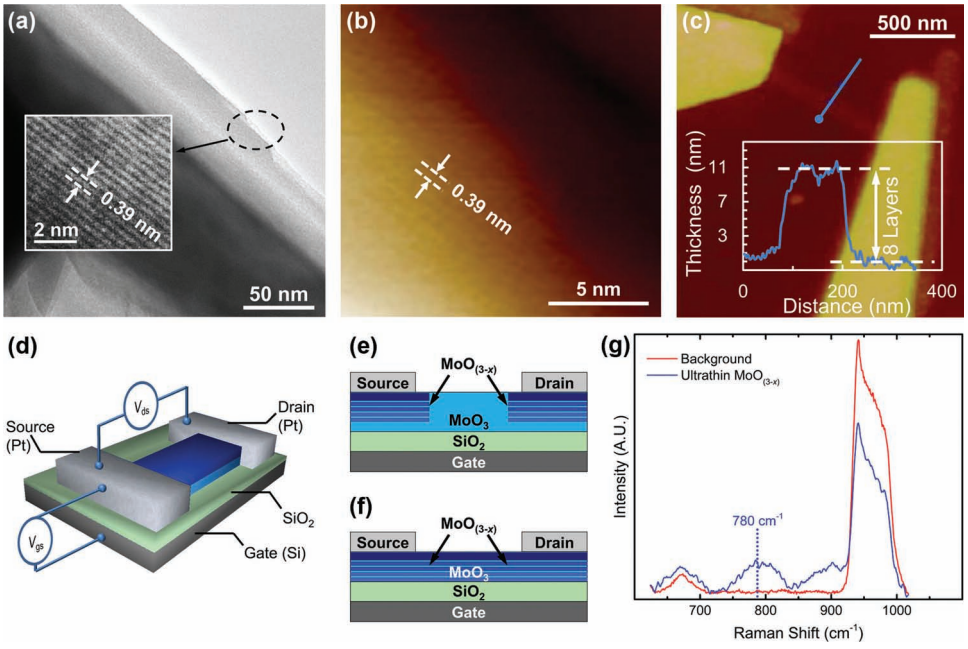

Figure 2. Characterization of MoO_3 and $MoO_{(3-x)}$ flakes and the configuration of FETs. (a) TEM image of an exfoliated MoO_3 crystal with inset showing magnified lattice arrangement with parameters matching α-MoO_3 (ICDD No: 35-0609). (b) STM image of a sub-stoichiometric $MoO_{(3-x)}$ flake with similar lattice spacing to that of MoO_3 and inset of (a). This also indicates conductivity of the flake. (c) AFM scan of a MoO_3 FET fabricated by electron beam direct writing with the corresponding thickness profile of the flake. The measured thickness of ~11 nm indicates the presence of eight fundamental layers in MoO_3. (d) Illustration of *I–V* characterization setup. (e,f) Cross-sectional schematic of formation of sub-stoichiometric states in MoO_3 as a result of electron beam writing and intercalation. (g) Micro-Raman spectra of the MoO_3 flake in (c) with broad peak at 780 cm^{-1} (absent in background measurement of substrate) indicating presence of $MoO_{(3-x)}$.

and Methods in the supporting information for details of the fabrication process. Figure 2c depicts the AFM image of a FET with a ~11 nm flake comprised of 8 fundamental atomic layers of MoO_3, each with the thickness of approximately 1.4 nm.[11] This was the thinnest flake, which could be incorporated into a device, as our electron beam had a detrimental effect on the formation of contacts to thinner samples. Many devices were fabricated with varying MoO_3 thicknesses from several microns to the minimum of 11 nm, with and without the application of electron beam lithography, to benchmark the performance of the devices and contacts (Figures S10 and S12).

The material in the structure of the FETs were reduced (Figures 2d–2f), generating oxygen vacancies resulting in the formation of sub-stoichiometric $MoO_{(3-x)}$. Raman spectra of the 2D layer, used in the FETs (Figure 2g), also contains the expected Raman peak shift feature at 780 cm^{-1}, corresponding to that observed in $MoO_{(3-x)}$ (Figure 1c).

Current–voltage (*I–V*) characteristics of the FETs were obtained for a range of back-gate voltages as shown in **Figure 3**. Carrier mobility of the device was calculated using the following equation:[22]

$$\mu = \frac{\Delta I_{DS}}{\Delta V_{GS}} \times \frac{l}{C \times w \times V_{DS}} \quad (2)$$

where $\Delta I_{DS}/\Delta V_{GS}$ is the transconductance defined by the drain–source current (I_{DS}) and the gate–source voltage (V_{GS}), l = 800 nm is the channel length, w = 80 nm is the channel width, $C = 1.15 \times 10^{-8}$ F cm^{-2} is capacitance per unit area of the gate dielectric material, and V_{DS} = 20 mV is the drain–source voltage. The carrier mobility was calculated from the *I–V* curves to be >1100 cm^2 V^{-1} s^{-1} (See supporting information for detailed calculations). In this device the surface charge density was also estimated to be 1.73×10^{-8} C cm^{-2} (See supporting information for calculations). It is important to mention that the FETs could not be completely switched off. The intercalation process caused the top layer to become nearly metallic (discussed later), effectively reducing the ON/OFF ratio to $<10^3$ (Figure 3b). This near-metallic layer proved to be very effective for the injection of excess electrons, similar to high electron mobility transistor structures.[2] The gate modulation seems significant under small range of gate bias (from –2 to 2 V),[23] considering we have a very thick gate dielectric layer (300 nm of SiO_2).Temperature dependent mobility studies were conducted in the range of 20 to 100 °C, and compared to the theoretical calculations. The experimental values follow the theoretical trend (See supporting information). As described previously, the results show that acoustic scattering is the dominant effect in limiting the carrier mobility.

The enhanced performance of our FETs can be explained by the physics of high-κ layer dominating the Coulomb scattering effect, as extracted from Equation 1. However the theoretical mobility is slightly larger than that of the measured. This can be due to the surface roughness of SiO_2 (Figure S14), which increases the roughness scattering effect.

Something which is of importance is the formation of near Ohmic contacts under the electron beam established Pt electrodes. Our Raman measurements show that the highly energetic beam produces a highly reduced $MoO_{(3-x)}$ layer under

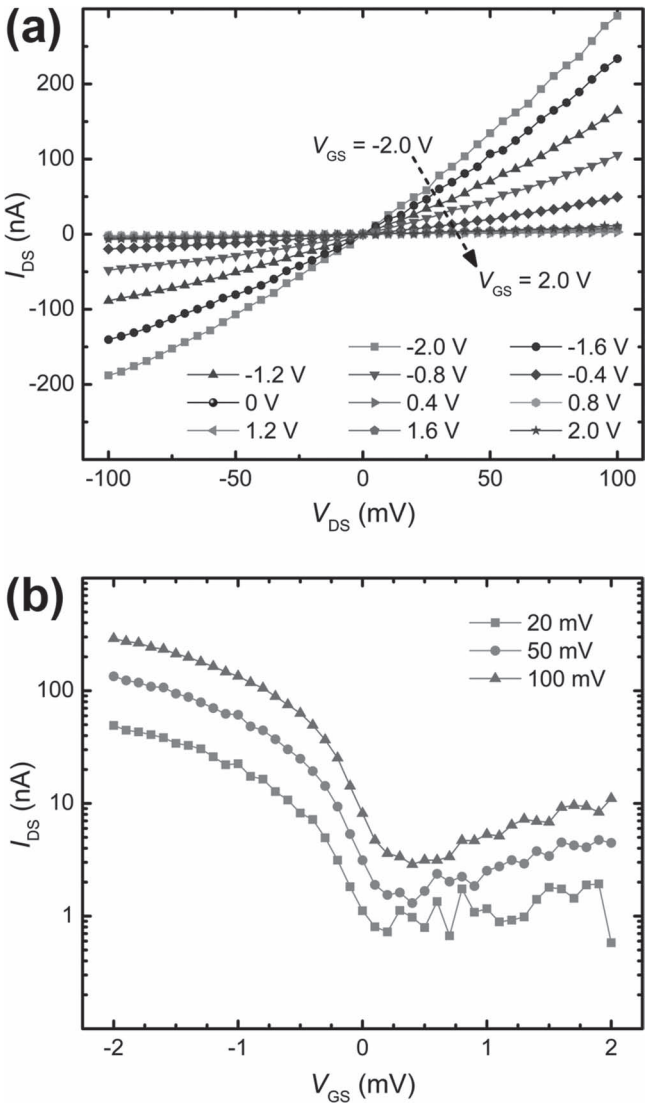

Figure 3. The experimental *I–V* characteristics of the MoO_3 FET. (a) I_{DS} vs. V_{DS} characteristics of the FET with varying back-gate voltages (V_{GS}) in steps of 0.4 V from –2 to +2 V. (b) Corresponding I_{DS}–V_{GS} curves of the FET acquired at V_{DS} values of 20, 50, and 100 mV.

and near the Pt electrodes, which is almost metallic (Figure S15). During the FET operation, electrons can be easily transferred from Pt to this near metallic layer, which can then be further injected down into the underneath layers through van der Waals gaps. This electronic charge transfer from the conducting non-stoichiometric layer to neighboring more stoichiometric layers has been confirmed by density functional theory (DFT) simulations. As shown in **Figure 4**, the conduction states in neighbor layers L1, L2, L1′ and L2′ are pushed down below the Fermi level resulting in reduced energy gaps between these layers' valence states and conduction states (Figures S16 and S17). Thus, while the lattice matching remains perfect, the free charge carriers can be exchanged between the layers and eventually guided within the planes.

We showed that using the Born approximation equation, one can predict and design the electronic characteristics of a 2D

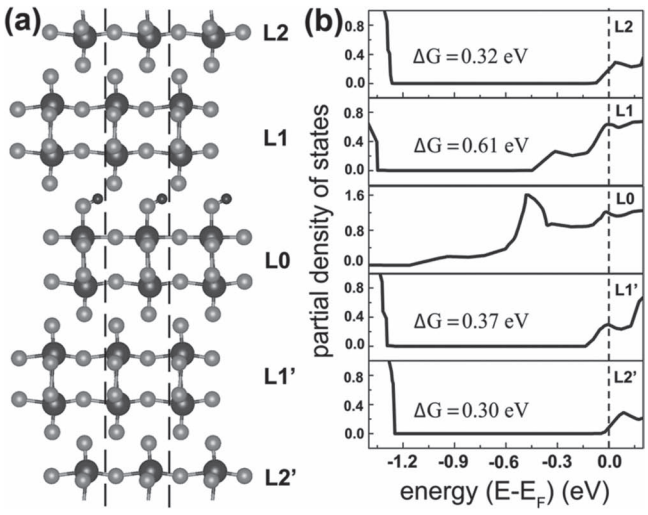

Figure 4. Density functional theory (DFT) simulations of charge injection in layered α-MoO_3. (a) Schematic illustrating ball and stick atomic model of bulk α-MoO_3 with large, medium and small spheres denoting Mo, O, and H atoms, respectively. Only five MoO_3 layers are shown for clarity: Layer L0, where hydrogen atoms are adsorbed near the oxygen atom located at the corner of MoO_3 octahedra, nearest layers L1 and L1′, and next-nearest layers L2 and L2′. (b) Partial density of states projected on each atomic site and summed for each layer. For nearest and next-nearest layers, ΔG denotes reduction in the band gap from their bulk, defect-free state.

semiconducting metal oxide. We theoretically demonstrated that the 2D α-MoO_3 has high carrier mobility. However, the natural bandgap of α-MoO_3 is so wide, that it does not thermionically generate enough charge carriers, required for the operation of FETs. The Coulomb charges were used in order to reduce the bandgap of the 2D MoO_3. These charges can be introduced by either intercalated H^+, or the reduction of MoO_3 to $MoO_{(3-x)}$. This process produces gap states, resulting in the reduction of the materials bandgap. In low-κ materials, the incorporation of Coulomb charges decreases the carrier mobilities due to the Coulomb scattering effect. However, in high-κ $MoO_{(3-x)}$ the Coulomb scattering effect is minimized and the carrier mobility still remains high. Additionally, the Coulomb charges also generate near Ohmic contacts at the drain and source electrodes, that allow the injection of electrons into the FET channel.

Here, we exfoliated α-MoO_3 and reduced to $MoO_{(3-x)}$. By implementing a ~11 nm thick 2D high-κ semiconductor, we were able to reduce the Coulomb scattering potential effect significantly, which resulted in the carrier mobility values >1100 $cm^2\ V^{-1}\ s^{-1}$ that readily exceeded those of doped and low dimensional silicon[24] and that of single layer MoS_2[10] (see supporting information for a comparison of the mobilities for different materials). Well known procedures for the large scale synthesis and manipulation of 2D MoO_3 and many other transition metal oxides,[13] as well as their relative abundance in nature and their great optical and catalytic properties, renders them ideal building blocks of future electronic and optical devices, sensors, and integrated circuits. It is also suggested that the work to be expanded to other low dimensional MoO_3 structures, such as nanorods and nanobelts in the future.[25]

Supporting Information

Supporting Information is available from Wiley Online Library or from the author.

Acknowledgements

SS and MB acknowledge the Australian Post-Doctoral Fellowships from the Australian Research Council through Discovery Projects DP110100262 and DP1092717, respectively. SS and KKZ acknowledge the Australian Research Council for equipment funding through the Linkage, Infrastructure, Equipment, and Facilities Grant LE100100215. The work was partially supported by the CSIRO Sensors and Sensor Networks Transformational Capability Platform and CSIRO Materials Science and Engineering Division. JD and NM thank Philip Chan, the Monash HPC cluster, and the MASSIVE and NCI facilities funded by the Australian Government for their support for computational resources. The authors also would like to acknowledge the facilities, and scientific and technical assistance, of the Australian Microscopy & Microanalysis Research Facility at the RMIT Microscopy & Microanalysis Facility, at RMIT University.

Received: August 14, 2012
Revised: September 7, 2012
Published online: October 23, 2012

[1] a) A. H. C. Neto, K. Novoselov, *Rep. Prog. Phys.* **2011**, *74*, 082501; b) J. A. Rogers, M. G. Lagally, R. G. Nuzzo, *Nature* **2011**, *477*, 45.
[2] T. Ando, A. B. Fowler, F. Stern, *Rev. Mod. Phys.* **1982**, *54*, 437.
[3] K. Takei, H. Fang, S. B. Kumar, R. Kapadia, Q. Gao, M. Madsen, H. S. Kim, C. H. Liu, Y. L. Chueh, E. Plis, S. Krishna, H. A. Bechtel, J. Guo, A. Javey, *Nano Lett.* **2011**, *11*, 5008.
[4] E. H. Hwang, S. Das Sarma, *Phys. Rev. B* **2008**, *77*, 235437.
[5] K. S. Novoselov, A. K. Geim, S. V. Morozov, D. Jiang, Y. Zhang, S. V. Dubonos, I. V. Grigorieva, A. A. Firsov, *Science* **2004**, *306*, 666.
[6] J. S. Jie, W. J. Zhang, K. Q. Peng, G. D. Yuan, C. S. Lee, S. T. Lee, *Adv. Funct. Mater.* **2008**, *18*, 3251.
[7] L. Y. Jiao, X. R. Wang, G. Diankov, H. L. Wang, H. J. Dai, *Nat. Nanotechnol.* **2010**, *5*, 321.
[8] L. Y. Jiao, L. Zhang, X. R. Wang, G. Diankov, H. J. Dai, *Nature* **2009**, *458*, 877; X. L. Li, X. R. Wang, L. Zhang, S. W. Lee, H. J. Dai, *Science* **2008**, *319*, 1229.
[9] K. S. Novoselov, D. Jiang, F. Schedin, T. J. Booth, V. V. Khotkevich, S. V. Morozov, A. K. Geim, *Proc. Natl. Acad. Sci. U. S. A.* **2005**, *102*, 10451.
[10] B. Radisavljevic, A. Radenovic, J. Brivio, V. Giacometti, A. Kis, *Nat. Nanotechnol.* **2011**, *6*, 147.
[11] K. Kalantar-zadeh, J. S. Tang, M. S. Wang, K. L. Wang, A. Shailos, K. Galatsis, R. Kojima, V. Strong, A. Lech, W. Wlodarski, R. B. Kaner, *Nanoscale* **2009**, *2*, 429.
[12] K. Kalantar-zadeh, A. Vijayaraghavan, M. H. Ham, H. D. Zheng, M. Breedon, M. S. Strano, *Chem. Mat.* **2010**, *22*, 5660.
[13] M. Osada, T. Sasaki, *Adv. Mater.* **2012**, *24*, 210.
[14] Y. Yoon, K. Ganapathi, S. Salahuddin, *Nano Lett.* **2011**, *11*, 3768.
[15] a) R. Naouel, H. Dhaouadi, F. Touati, N. Gharbi, *Nano-Micro Lett.* **2011**, *3*, 242; b) E. A. I. Saad, *J. Optoelectron. Adv. Mater.* **2005**, *7*, 2743.
[16] a) C. S. Hwang, *J. Appl. Phys.* **2002**, *92*, 432; b) K. Natori, D. Otani, N. Sano, *Appl. Phys. Lett.* **1998**, *73*, 632.
[17] A. Bouzidi, N. Benramdane, H. Tabet-Derranz, C. Mathieu, B. Khelifa, R. Desfeux, *Mater. Sci. Eng. B-Solid* **2003**, *97*, 5.

[18] X. K. Hu, Y. T. Qian, Z. T. Song, J. R. Huang, R. Cao, J. Q. Xiao, *Chem. Mater.* **2008**, *20*, 1527.
[19] X. W. Sha, L. Chen, A. C. Cooper, G. P. Pez, H. S. Cheng, *J. Phys. Chem. C* **2009**, *113*, 11399.
[20] J. Z. Ou, J. L. Campbell, D. Yao, W. Wlodarski, K. Kalantar-zadeh, *J. Phys. Chem. C* **2011**, *115*, 10757.
[21] J. W. Rabalais, R. J. Colton, A. M. Guzman, *Chem. Phys. Lett.* **1974**, *29*, 131.
[22] D. K. Schroder, *Semiconductor Material and Device Characterization*, Wiley, **1990**.
[23] L. T. Liu, S. B. Kumar, Y. Ouyang, J. Guo, *IEEE Trans. Electron Devices* **2011**, *58*, 3042.
[24] S. M. Sze, K. N. Kwok, *Physics of Semiconductor Devices*, Wiley **2007**.
[25] a) J. S. Chen, Y. L. Cheah, S. Madhavi, X. W. Lou, *J. Phys. Chem. C* **2010**, *114*, 8675; b) Z. Wang, S. Madhavi, X. W. Lou, *J. Phys.Chem. C* **2012**, *116*, 12508.